Donor-cluster arrays as a quantum computer in silicon

Shihang Zhang,^{1,2} Chunhui Zhang,^{1,2} Guanyong Wang,² Tao Xin,² Guangchong Hu,^{2,3,*} Yu He,^{2,3,†} and Peihao Huang^{2,3,‡}

¹Shenzhen Institute for Quantum Science and Engineering, Southern University of Science and Technology, Shenzhen 518055, China ²International Quantum Academy, Shenzhen 518048, China ³Shenzhen Branch, Hefei National Laboratory, Shenzhen, 518048, China. (Dated: October 6, 2025)

Significant advances in silicon spin qubits highlight the potential of silicon quantum dots for scalable quantum computing, given their compatibility with industrial fabrication and long coherence times. In particular, phosphorus (P)-doped spin qubits possess excellent coherence and have demonstrated high-fidelity two-qubit gates exceeding 99.9%. However, scaling P-donor systems is challenging due to crosstalk caused by the uniformity of individual P donors and the low tolerance for imprecise atomic placement. Stochastic placement can lead to multiple donors located within a small region (diameter < 3 nm), forming a so-called donor cluster. Notably, in cluster-based systems, high-fidelity multi-qubit quantum gates and all-to-all connectivity have recently been demonstrated experimentally on nuclear spin qubits. In this work, we propose a scalable cluster-array architecture for nuclear spin qubits and a corresponding control protocol. We analyze crosstalk-induced errors, a major error source, during primitive operations under various parameters, showing that they can be suppressed through device design and control optimization. We evaluate the fidelities of intra- and inter-cluster multi-qubit gates between nuclear spins, confirming the feasibility of our architecture and establishing design requirements and parameter targets. The local all-to-all connectivity within clusters provides unique flexibility for quantum error correction. Our scalable scheme provides a path toward large-scale spin-based quantum processors.

I. INTRODUCTION

Silicon quantum dots represent a promising pathway to scalable quantum computation, uniting industrial manufacturability with long spin qubit coherence time [1-7]. When fabricated in isotopically purified ²⁸Si, these devices eliminate the magnetic noise associated with ²⁹Si. Combined with the weak spin-orbit coupling of silicon, yields electron-spin relaxation times T_1 in excess of 1 s and dephasing times $T_2^* > 100 \text{ ms}$ [3]. Complementarymetal-oxide-semiconductor (CMOS) compatible fabrications have already delivered single-qubit gates with a fidelity of 99.85% and two-qubit gates with a process fidelity of 98.92%, all operating above 1 K [6, 8]. Recent demonstrations of three-, four- and six-qubit processors that incorporate on-chip resonators, cryo-CMOS multiplexers, and single-electron transistors for dispersive readout confirm that the foundational ingredients for a silicon-based quantum computer are now in place [9– 12].

Phosphorus (P)-doped silicon is another major technical route with distinct benefits. Its 31 P donor nucleus (I=1/2) experiences a 117 MHz hyperfine (HF) coupling to its bound electron, which is three orders of magnitude stronger than the dipolar coupling between neighboring donors. This interaction permits universal control of the nuclear spin via the electron:

electron-spin-resonance (ESR) pulses on the electron enable multi-qubit gates among the nuclear spins [13–15], while nuclear-magnetic-resonance (NMR) pulses address the nucleus directly. Furthermore, the nuclear wave function's tight localization on the 31 P core makes the donor nuclear spin immune to electric field noise. This leads to a reported T_2 exceeding 30 s in enriched 28 Si, making 31 P the longest-lived single qubit in silicon [5]. Coupling two donors through their overlapping electron orbitals produces exchange coupling above megahertz, enabling fast entanglement between the electron spins. This electron-mediated approach has recently been used to demonstrate high-fidelity nuclear-nuclear multi-qubit gates in a two-neighboring donor cluster system [13–16], with two-qubit gate fidelities reaching 99.9% [15].

Despite these advances, the approaches [17, 18] to scaling a single-donor array are hindered by several interrelated challenges. First, fabrication imperfections, such as the potential failure of donor incorporation at the target site [19] and spatial variations that modulate the valley-orbit splitting [20, 21]. Second, quantum-control and readout limitations, including ionization shock induced by single-electron charge tunneling during readout [22], frequency crowding and RF crosstalk caused by unresolvable ESR spectrum from donors with similar hyperfine couplings, the demand for sequential SWAP chains due to sparse connectivity when compiling quantum circuits [11], and the decomposition of multi-qubit gates into many two-qubit primitives. Third, scalability barriers, including the high wiring density resulting from multiple DC gates, coupled SET islands, and RF lines required per qubit [17], with the risks exceeding the

^{*} hugc@iqasz.cn

[†] hey@iqasz.cn

[‡] huangph@iqasz.cn

thermal budget of dilution refrigerators.

Here, we propose a fundamental re-imagining: turning these challenges into assets by embracing, rather than combating, fabrication imperfections through clusterarray-based architectures. In our proposal, rather than using a single P atom at each lattice site, we encode a logical qubit in a cluster consisting of a few (N) donors. The delocalized electron of this cluster creates 2^N discrete HF lines, mitigating frequency crowding for nuclear spins within a cluster. Notably, unexpected fluctuations in the number of donors within a cluster have no significant effect on the feasibility of the cluster-based qubit scheme (see Appendix C). Furthermore, collective superexchange couples every nucleus within the cluster, delivering all-to-all connectivity among the nuclear spins in neighboring clusters and proving the potential to reduce two-qubit gate counts in the circuit compilation of quantum algorithms [23]. As demonstrated in a recent experiment, leveraging this inherent connectivity, genuine inter-cluster entanglement of up to eight qubits has been achieved [15].

While cluster-based spin operations have been demonstrated [14, 15], a scalable architecture for a clusterbased quantum computer has yet to be established. Moreover, achieving fault-tolerant quantum computing requires compatible quantum error correction (QEC) schemes. Our architecture aims to provide a systematic solution addressing both of these demands. Two key aspects of our solution are worth noting. The first is the utilization of the inherent all-to-all connectivity in each cluster [14] and the strongly biased noise in the qubits [5, 24]. This connectivity allows each cluster to serve as a reconfigurable building block for topological codes. For example, the XZZX surface code [25, 26] can be implemented on 1D cluster chains. Given the highly biased noise in silicon-based systems, this encoding provides effective error suppression [26]. Even with a noise bias value (the ratio of Z noise to the sum of Xand Y noise) of 10, the fidelity threshold for fault tolerance could be lower than 95% [25]. The second key aspect is frequency crowding mitigation, a major bottleneck for scaling cluster arrays. Although hyperfine (HF) randomness enables qubit-selective addressing, frequency crowding becomes unavoidable as the number of qubits increases. Therefore, the switchable exchange interaction [27–30] must be utilized to suppress this issue during intra-cluster operations.

Below, we present the theoretical framework and scalability analysis for this cluster-array-based paradigm. We show that HF heterogeneity enables crosstalk-free addressing fidelity >99%. Furthermore, intra-cluster multiqubit gates reach 99% fidelity, while inter-cluster multiqubit gates achieve 98% fidelity. Moreover, we show that an XZZX surface code can be implemented on a 1D cluster chain. By harnessing rather than eliminating fabrication randomness, donor clusters offer a compact, CMOScompatible path toward large-scale quantum processors in silicon.

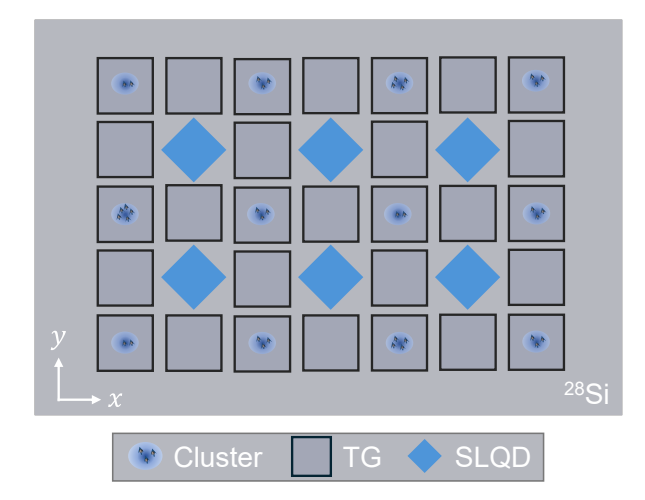


FIG. 1. Scalable cluster-based spin qubit scheme in ²⁸Si. Donor clusters are arranged into a two-dimensional array. Each donor cluster contains multiple P donors and one electron bound to them. Top gates (TGs) above the clusters are used to adjust the energy detuning between clusters. To achieve tunability of exchange interactions between neighboring electrons, the inter-cluster TGs is used to adjust tunneling. In a state-of-the-art device, the exchange interaction is tuned by adjusting detuning between clusters. Additionally, single-lead quantum dots (SLQDs) are incorporated between clusters for readout and loading of electrons.

II. SCALABLE CLUSTER-BASED SPIN QUBIT SCHEME

A. Architecture

The architecture of our proposed scalable cluster-based spin qubit scheme is shown in Fig. 1. Clusters containing multiple P-donors are arranged in a two-dimensional (2D) array. Each single-lead quantum dot (SLQD) is positioned at the center of a rectangular configuration of four clusters, enabling both electron spin readout and initialization [31]. Nuclear spins within clusters can also be initialized and measured via electron-assisted quantum non-demolition (QND) readout. Top gates (TGs) between adjacent clusters allow the turning on and off of the exchange interaction between confined electrons. Additionally, micromagnets (not depicted) placed outside the array generate magnetic field gradients to enhance spatial addressing of clusters.

A static magnetic field is applied along the \hat{z} -direction perpendicular to the device. The nuclear spin-up $(|\uparrow\rangle)$ and spin-down $(|\downarrow\rangle)$ states of the P-donor are encoded as the $|0\rangle$ and $|1\rangle$ states of the data qubit, while the electron spin states serve as the ancilla qubit. When qubit operations are required, global alternating magnetic fields are applied to drive the spin qubits. Specifically, single-qubit gates are performed via NMR drivings, while two-qubit gates are implemented via conditional ESR operations. The exchange interaction is switched on solely for intercluster operations and remains off during intra-cluster

operations to avoid introducing extra errors.

In the following, the system Hamiltonian of a single cluster is introduced first. Next, Sec. II C outlines the tuning-up procedure for the cluster-based qubit scheme. The overall qubit operation protocol is then described, beginning with the initialization and readout of nuclear spin qubits in Sec. II C. Intra-cluster operations based on NMR and ESR are then introduced in Sec. II D, and inter-cluster operations and crosstalk errors arising from frequency crowding are discussed in Sec. II E. Based on the above discussion, the universal gate set for the cluster-based qubit scheme is presented in Sec. II F.

B. System Hamiltonian

In Fig. 2(a), we take a 2P cluster and a 2P-3P cluster pair in the cluster array as examples to demonstrate qubit control protocols for the scalable cluster-based spin qubit scheme. The upper part of Fig. 2(a) shows the magnetic field gradient generated by a micromagnet. For a single cluster shown in Fig. 2(b), the Hamiltonian can be expressed as

$$H_{\text{cluster}} = \gamma_e \mathbf{B} \cdot \mathbf{S} + \sum_i \gamma_n \mathbf{B} \cdot \mathbf{I}_i + \sum_i A_i \mathbf{S} \cdot \mathbf{I}_i, \quad (1)$$

where the first two terms correspond to the Zeeman Hamiltonians of the electron spin and the nuclear spins, respectively. **S** and \mathbf{I}_i are spin operators of the electron spin and nuclear spins, respectively. $\gamma_n = -17.41$ MHz/T and $\gamma_e = 27.97$ GHz/T are the gyromagnetic ratios of a nuclear spin and an electron spin. Without time-dependent drives, only the \hat{z} -axis static magnetic field B_0 remains, inducing Zeeman splittings of the electron spin and the nuclear spins.

The last term of H_{cluster} describes the HF interaction between the electron spin and the nuclear spins. The HF interaction strength A_i depends on the overlap between the electron wavefunction and the corresponding nucleus. Typical values of A_i for P donors within a cluster range from hundreds of kHz to hundreds of MHz [15, 32]. Since the electron spin Zeeman splitting (on the order of tens of GHz) substantially dominates the HF interaction strength, the flip-flop between electron spin and nuclear spin is suppressed. Moreover, the coherence time of the nuclear spin is longer than that of the electron spin. Therefore, only the ZZ term in the HF interaction remains non-negligible. The energy of a given state is increased by A/4 when the electron spin and nuclear spin are parallel, while it is decreased by A/4 when they are antiparallel. The energy levels of a 2P cluster are illustrated in the middle of Fig. 2(d). The modification of energy levels by the HF interaction enables the implementation of addressable single-qubit gates and low-overhead multi-qubit gates within the cluster.

C. Tuning up of the system

The first step for system tuning up is the charge filling within each cluster. There are two key voltage working points that must be pre-calibrated: one is a region where the exchange interaction is turned off, allowing both electron spin readout [31] and the subsequent intracluster calibration process; the other is where exchange interaction between neighboring clusters is turned on, which enables inter-cluster quantum operations. Moreover, given the inherent complexity of the charge stability diagram for multi-cluster devices, a complementary approach combining virtual gates [33, 34] and charge transition simulations [35] is essential for accurate characterization.

Based on the above, the following tuning-up procedure is performed under two stages: one with the exchange interaction off, and the other with it on. (i) Initially, the exchange interaction is turned off, allowing each cluster to be treated as a single cluster. The ESR and NMR frequencies for a single cluster are characterized as follows: first, an adiabatic ESR sweep is performed, from which the ESR frequencies and HF interactions can be extracted. These results are subsequently used to confirm the corresponding NMR frequencies. Using the measured ESR and NMR frequencies along with the protocol in Refs. [14], the spin system can be initialized into a specific quantum state, and the exemplary initialization circuit is shown in Fig. 3(a). This enables the calibration of NMR-based single-qubit and ESR-based intra-cluster multi-qubit gates. The entire procedure described above completes the calibration for a single cluster. Furthermore, the development of RF-multiplexing readout [10, 36] and multi-tone driving [37] techniques enables the simultaneous calibration of multiple clusters (with exchange interaction off), offering the potential to significantly accelerate the overall process. (ii) When the exchange interaction is turned on, the two adjacent clusters are coupled. In this case, each cluster pair can be treated as a "large single cluster" (as shown in Fig. 2(d)) and undergoes the same calibration procedure. Since each inter-cluster operation only requires activating the exchange interaction between the corresponding adjacent clusters, it is only necessary to pre-calibrate all adjacent cluster pairs. Thus, inter-cluster multi-qubit gates can be calibrated in the same way as above.

D. Intra-cluster operations using NMR and ESR

In the qubit operation stage, all quantum gates for the cluster-based qubit scheme are implemented using two primitive operations: NMR driving and conditional ESR driving. For simplicity, we use a 2P-1P pair as an example to illustrate the qubit operations. Addressable and arbitrary single-qubit operations can be achieved by applying NMR pulses at specific resonance frequencies. Since electron spins are initialized to the spin-down

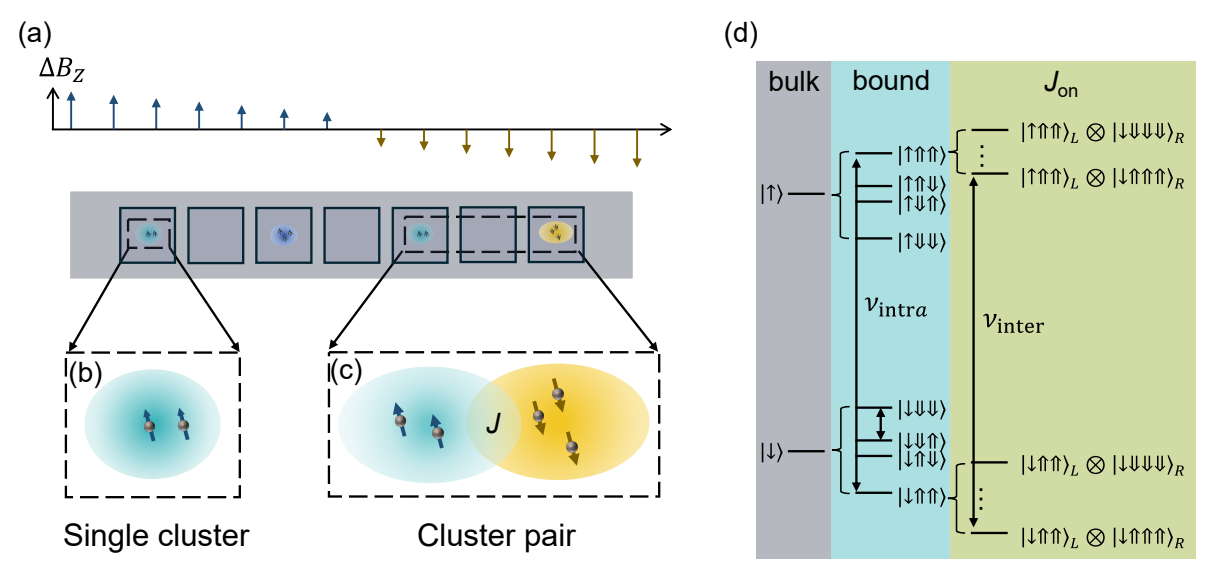


FIG. 2. Addressability in the scalable cluster-based qubit scheme. (a) The clusters are arranged linearly with a longitudinal magnetic field gradient ΔB generated by the micromagnet. The spatial distribution of the magnetic field gradient ensures frequency discrimination between qubits in distinct donor clusters. (b) Nuclear spin qubits within a cluster are coupled to a single confined electron via hyperfine interactions. (c) The nuclear spin qubits, coupled via effective exchange interaction between electron spins, belong to adjacent 2P and 3P clusters, respectively. (d) Schematic diagram of electron spin energy levels. The spin-up and spin-down states of the electron are split under the magnetic field, with the corresponding splitting magnitude determining the ESR driving frequency. When the electron is confined to a 2P cluster, its spin energy levels undergo further splitting due to hyperfine interactions with the two donors. When the electron spin couples with the neighboring electron spin, its energy levels further split according to the nuclear spin states of the adjacent cluster. The electron in the right cluster is assumed to be initialized in the spin-down state. For simplicity, the energy levels corresponding to the spin-up state of the right electron are not included.

state $|\downarrow\rangle$, the qubit frequency of the *i*-th nuclear spin becomes $\hbar\omega_i = \gamma_n B_0 + A_i/2$. Consequently, nuclear spin frequencies can be resolved by their distinct hyperfine coupling A_i . Due to randomness in donor placement, the HF strengths of donors within a device typically exhibit intrinsic differences. The difference enables the addressability of single-qubit operations. However, in a large-scale qubit device, the difference might be quite small. In such cases, the frequency differences provided by the magnetic field gradient ΔB are required to further achieve qubit addressing.

Similarly, electron spin can be manipulated by a conditional ESR, which depends on the nuclear spin combination states. The ESR spectrum of a 2P cluster can be understood by referring to the results in the region around J=0 in Fig. 3(b). The ESR frequencies split into four groups, corresponding to the four basis states formed by the two nuclear spins in the 2P cluster. An up (down) state of the corresponding nuclear spin N_i raises (lowers) the ESR frequency by $A_i/2$. Thus, the differences between these frequencies are determined by the HF interaction strengths of the two nuclear spins. Consequently, a 2π -rotation can be performed conditional on a specific combined nuclear spin state, as shown in Fig. 3(c). Performing a 2π rotation of the electron spin on a specific state accumulates a π phase on that state while preserving its population, effectively realizing a multi-qubit CZ gate [13, 14]. Furthermore, when combined with singlequbit operations, a CNOT/Toffoli gate between nuclear spin qubits can be implemented. Therefore, both single-qubit and multi-qubit gates within a single cluster can be achieved with the assistance of the bound electron.

E. Inter-cluster operations using ESR

The mediating role of electrons can be further exploited to enable inter-cluster multi-qubit operations between adjacent clusters. The Hamiltonian for a two-cluster system is as follows:

$$H_{2C} = H_{\text{cluster,L}} + H_{\text{cluster,R}} + J\mathbf{S_L} \cdot \mathbf{S_R},$$
 (2)

where $H_{\text{cluster,L(R)}}$ is the single-cluster Hamiltonian for the left (right) cluster, $S_{\text{L(R)}}$ is the spin operator for the left (right) electron, and J is the strength of the exchange interaction between the two electrons. When the exchange coupling is turned on, the spin states are further split, as shown in Fig. 2(d). This causes the driving frequency of the left electron spin to depend on the nuclear spin configuration in the right cluster, and vice versa. Considering a 2P-1P pair with HF strengths $[A_{1L}, A_{2L}, A_{1R}] = [50, 150, 110]$ MHz, the ESR spectrum of the electron in the left cluster is plotted as a function of J in Fig. 3(b). The magnetic field B_0 is set to 1.35 T. As the exchange coupling increases from zero, the four groups of ESR frequencies progressively split into solid and dashed

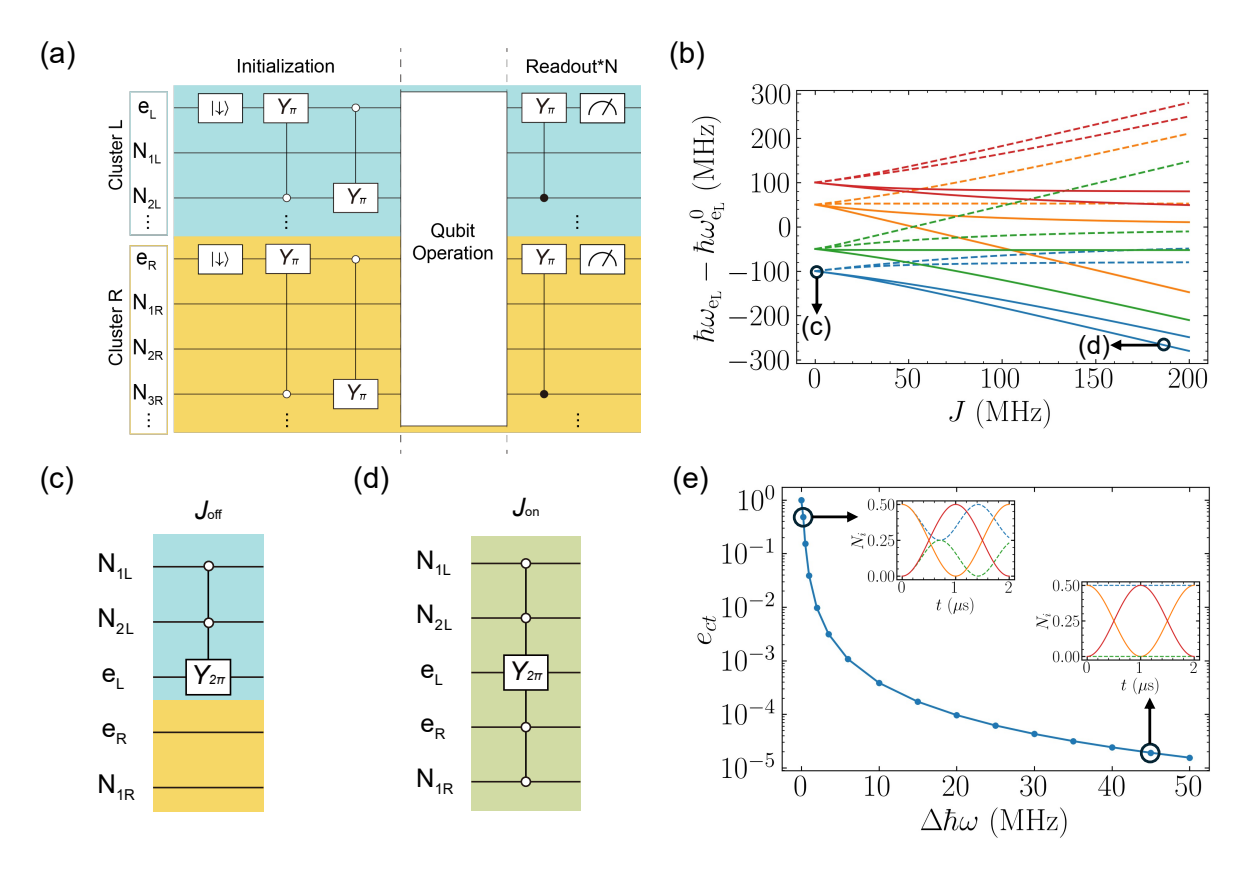


FIG. 3. Schematic of qubit initialization, readout, and ESR-based CZ gate. (a) Circuit for the control protocol includes gubit initialization, operation, and readout. Detailed sequences for the initialization and readout of a specific nuclear spin in each cluster are shown. Taking $N_{2L} \mid \downarrow \downarrow \rangle$ initialization as an example, the electron is initially prepared to $\mid \downarrow \rangle$, then all ESR π pulses involving N_{2L} are applied to flip the corresponding electron spin; followed by the NMR π pulse conditional on the electron spin being in $|\downarrow\rangle$. The three steps above constitute N_{2L} $|\downarrow\downarrow\rangle$ initialization procedure. The final nuclear spin readout, also implemented by a bound electron, constitutes a quantum non-demolition (QND) measurement. This property enables repeated measurements to suppress SPAM errors. (b) The ESR frequency of the electron in the left cluster is shown as a function of the exchange interaction strength J. Here, a 2P-1P pair is taken as an example. Near J=0, the frequencies splits into four groups depending on the nuclear spin states in the left cluster: $|\downarrow\downarrow_1 L \downarrow\downarrow_2 L\rangle$ (red), $|\uparrow\uparrow_1 L \downarrow\downarrow_2 L\rangle$ (orange), $|\downarrow\downarrow_1 L \uparrow\uparrow_2 L\rangle$ (green), and $|\uparrow_{1L}\uparrow_{2L}\rangle$ (blue). The solid curves correspond to the electron spin in the right cluster being $|\downarrow_{R}\rangle$, while the dashed curves represent the electron spin being $|\uparrow_R\rangle$. The splitting between frequencies with the same color and line style depends on the nuclear spin state on the right. (c) Intra-cluster CZ operation based on a conditional 2π ESR rotation with $J = J_{\text{off}}$ [(c) in Figure (b)]. (d) Inter-cluster CZ operation based on a conditional 2π ESR rotation with $J = J_{\rm on}$ [(d) in Figure (b)]. (e) The crosstalk error during 2π ESR rotations is plotted as a function of detuning between driving frequency and the off-resonant frequency. The insets show the time evolution of the electron spin population under a large detuning (45 MHz) and a small detuning (0.25 MHz). Here, the solid curves correspond to the target nuclear spin state, while the dashed curves represent a non-target nuclear spin state.

lines, corresponding to the $|\downarrow_{\rm R}\rangle$ and $|\uparrow_{\rm R}\rangle$ states of the right electron, respectively. When J is sufficiently strong, these split lines further divide into two lines, corresponding to the adjacent nuclear spin being in the $|\uparrow_{\rm 1R}\rangle$ and $|\downarrow_{\rm 1R}\rangle$ states. Consequently, a 2π -rotation on the electron spin can be performed conditional on the combined state of nuclear spins in two neighboring clusters, as exemplified in Fig. 3(d). Similar to the intra-cluster case, inter-cluster multi-qubit CZ gates (Fig. 3(d)) and Toffoli gates can be implemented using the conditional ESR driving.

Both single-qubit and two-qubit gates rely on the frequency differences induced by the HF interactions. This is particularly critical for ESR-based multi-qubit gates,

as the faster ESR operation demands larger frequency detuning to suppress crosstalk error. To illustrate the impact of frequency detuning on crosstalk error, we take a 2P cluster as an example. When performing a 2π ESR rotation conditional on the $|\uparrow_{1L}\uparrow_{2L}\rangle$ state, the off-resonant driving on the electron spin conditioned on the $|\downarrow_{1L}\uparrow_{2L}\rangle$ state may be induced. By performing simulations based on the master equation (see Supplementary Materials), the crosstalk error during the ESR operation is plotted as a function of detuning $\Delta\hbar\omega$ between the ESR frequency conditioned on the target state and that on another state in Fig. 3(e). The Rabi frequency of the ESR operation is set to 0.5 MHz. With a small detuning $(\Delta\hbar\omega = 0.25 \text{ MHz})$, the amplitude of the electron spin state population

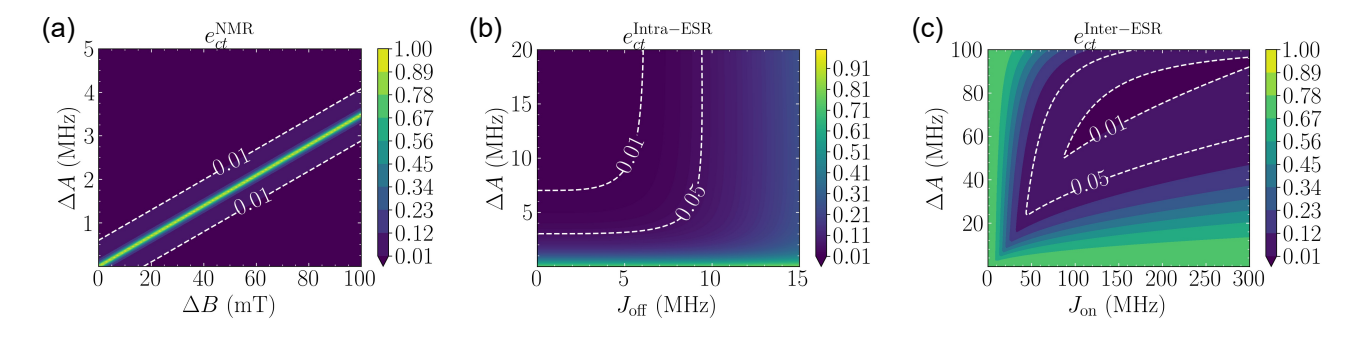


FIG. 4. Addressability for NMR, intra-cluster ESR and inter-cluster ESR operations. (a) The crosstalk error rate e_{ct}^{NMR} of the NMR operation is plotted as a function of the magnetic field gradient ΔB and the minimum hyperfine difference ΔA . (b) The crosstalk error rate $e_{ct}^{\mathrm{Intra-ESR}}$ of the intra-cluster ESR operation is plotted as a function of residual exchange interaction J_{off} and minimum hyperfine difference ΔA . (c) The crosstalk error rate $e_{ct}^{\mathrm{Inter-ESR}}$ of the inter-cluster ESR operation is plotted as a function of activated exchange interaction J_{on} and minimum hyperfine interaction difference ΔA .

under off-resonant driving is close to that under resonant driving, resulting in a strong crosstalk error. In contrast, with a large detuning ($\Delta\hbar\omega=45$ MHz), the off-resonant driving of the electron spin is strongly suppressed. The corresponding crosstalk error rate is effectively reduced.

Mitigating frequency crowding is crucial for enhancing the scalability of qubit architectures. The randomness in HF interaction strengths naturally gives rise to a fundamental frequency distribution. Due to the stochastic placement of donors within clusters, the HF interaction strengths can vary significantly for different donor configurations and donor numbers. As discussed in Appendix C, by simulating with 1000 samplings, the feasible number of donors within a cluster ranges from 2 to 11. The average number is 4.3 (1.5). In such cases, the HF interaction strength distributions generally span a range from hundreds of kHz to hundreds of MHz. For largerscale quantum systems (containing hundreds of qubits), hyperfine interactions alone are insufficient to ensure frequency differentiation. Therefore, our scalable clusterbased qubit architecture incorporates micromagnets to induce magnetic field gradients, enabling addressability of clusters. However, frequency crowding may still be unavoidable. This can be mitigated through the control protocol design to prevent crosstalk, as discussed in the next section. Alternatively, affected gubits may be initialized but left idle during operations to avoid the crosstalk issue.

F. Universal gate set

For cluster-based nuclear spin qubits, arbitrary single-qubit gates based on NMR and multi-qubit CZ-type gates based on conditional ESR can be natively implemented. The specific form of the multi-qubit CZ gate is determined by the number of donors in the cluster. For a cluster consisting of N donors, the number of ESR pulses required to implement a K-qubit CZ gate is 2^{N-K} . The additional ESR pulses are applied to shield against the

control of irrelevant nuclear spins. For example, in a cluster with three donors, a three-qubit CZ gate can be natively implemented, whereas a CZ gate between two nuclear spins requires one more ESR pulse to realize. By combining two single-qubit H gates and one multi-qubit CZ-type gate, a Toffoli/CNOT-type gate between nuclear spins can be implemented. Similarly, When the number of donors within a cluster pair is M, the number of ESR pulses required for an L-qubit inter-cluster CNOT gate is 2^{M-L} . For example, in a 2P-3P cluster pair, a fivequbit inter-cluster Toffoli gate is implemented by two NMR pulses (H gates) and one ESR pulse. However, an inter-cluster CNOT gate requires two NMR pulses and eight ESR pulses. The difference in the number of pulses required for CNOT and Toffoli gates is a notable characteristic of cluster-based nuclear spin qubits. This necessitates tailored circuit design for algorithm demonstrations and QEC schemes.

Furthermore, a 'CXX' gate-defined as a CNOT gate with one control qubit and multiple target qubits-can also be constructed among nuclear spins. By performing H gates on the multiple target qubits in parallel, interleaved with conditional-ESR-based phase adjustments between the qubits, the CXX gate can be implemented in a time comparable to that of a Toffoli-type gate. The CXX gate plays an important role in QEC, particularly in logical state preparation and stabilizer operations. Its efficient implementation can significantly enhance the performance of QEC. The various multi-qubit gates described above ensure all-to-all connectivity among nuclear spin qubits both within a single cluster and across neighboring clusters. This local all-to-all connectivity is a distinctive feature of the cluster-based qubit scheme and offers advantages in QEC, which will be discussed in Sec. IV.

To summarize this section, we described the qubit operation protocol and gate set in our proposed scalable cluster-based spin qubit scheme. In particular, we discussed how to construct multi-qubit gates by leveraging the features and physical mechanisms of the cluster system. Crosstalk errors caused by frequency crowding will be one of the main factors limiting the gate performance. In the next section, we will examine the addressability of qubit operations in the proposed scalable scheme. We will also evaluate the gate performance under different parameter configurations to validate the feasibility of the scalable cluster-based scheme and identify an acceptable parameter regime.

III. PERFORMANCE OF MULTI-QUBIT GATES BETWEEN SPIN QUBITS IN CLUSTERS

A. Addressability of qubit operation

To systematically evaluate how HF interaction strengths, magnetic field gradients, and exchange interactions affect gate operations in our cluster-based architecture, we calculated crosstalk error rates during NMR, intra-cluster ESR, and inter-cluster ESR operations. The calculation of the crosstalk error is detailed in the Supplementary Material. The static magnetic field B_0 is set to 1.35 T. For simplicity, a 1P-2P pair is taken as an example. The minimum difference between HF interactions is defined as ΔA . The Rabi frequency is set to 30 kHz for NMR and 0.5 MHz for ESR, both higher than typical values to highlight the impact of crosstalk errors [15]. To ensure the result reflects the worst case, the crosstalk error is calculated using the smallest frequency difference among all possible frequency pairs.

As shown in Fig. 4(a), the crosstalk error for NMR operations is typically below 0.01. An error rate under this threshold requires an HF strength difference greater than 0.6 MHz, even without a magnetic field gradient ($\Delta B=0$). The reason for this low crosstalk is the weak driving strength of NMR, which minimizes off-resonant effects. However, the crosstalk error rate is significantly high along the diagonal bright line. This elevation occurs because the NMR frequency shift due to the HF interaction cancels out that from the magnetic field gradient, resulting in $\Delta\hbar\omega_{\rm NMR}=\frac{\Delta A}{2}-\gamma_n\Delta B=0$. The crosstalk error rate during intra-cluster ESR op-

The crosstalk error rate during intra-cluster ESR operation is shown in Fig. 4(b). Regions with low error rates (<0.05 and <0.01) are outlined by dashed white lines. To maintain the crosstalk error rate below 0.05, the HF difference ΔA should be larger than 3 MHz, and the residual exchange coupling $J_{\rm off}$ should be less than 9 MHz. A smaller ΔA induces frequency crowding, which exacerbates crosstalk issues. Additionally, a stronger $J_{\rm off}$ couples the electron spins, resulting in the ESR frequency depending on the nuclear spin polarization in the adjacent cluster. The frequency shift subsequently leads to off-resonant errors.

The result for inter-cluster ESR operation is plotted in Fig. 4(c). In the figure, only the frequency difference due to HF and exchange interaction is considered. In other words, degenerate frequencies caused by accidental coincidence are excluded from the analysis. To achieve

an an error rate below 0.05, the activated exchange interaction strength $J_{\rm on}$ should be stronger than 50 MHz, and the corresponding HF difference ΔA should exceed 25 MHz. A large ΔA ensures that ESR driving distinguishes specific nuclear spins, while a sufficiently strong $J_{\rm on}$ guarantees the addressability of nuclear spin states in adjacent clusters. Both the crosstalk error rate and the usable parameter range can be optimized further by employing weaker driving strengths or additional magnetic field gradients.

Even in the proposed scalable cluster-based gubit architecture, frequency crowding issues may still occur, particularly when implementing inter-cluster multi-qubit gates. To prevent crosstalk errors during direct intercluster CZ gate implementation, indirect approaches utilizing auxiliary operations can be employed. We present two indirect compilation schemes using the target CC-CCZ gate as an example. The first ESR-assisted scheme operates as follows [15]: First, a controlled π -rotation is applied on the left electron spin using its local nuclear spins as control qubits; then, a controlled 2π -rotation is performed on the right electron spin using both the left electron and right nuclear spins as joint controls; finally, the left electron spin is rotated back to its initial state through reversed operations. The second approach employs an NMR-assisted compilation scheme. method involves first applying a π -rotation to the nuclear spins, which enables the subsequent ESR 2π -rotation to effectively implement the target operation when condi-control states, followed by a final restoration π -rotation on the nuclear spins to complete the sequence. The ESR-assisted scheme requires fewer operations, while the NMR-assisted approach achieves higher precision in each individual operation. Based on results in the Supplementary Materials, the requirement for both the exchange coupling J and the HF difference ΔA in the ESR-assisted inter-cluster ESR scheme are much lower than those required for direct-implemented inter-cluster ESR operations. For NMR-assisted scheme, the requirement on the exchange interaction is relaxed, while the corresponding HF difference and error rate show a significant reduction.

B. Fidelity of multi-qubit gate

Nuclear-nuclear multi-qubit gates in the cluster-based scheme can be implemented via conditional ESR operations. In this section, we present the ESR-based multi-qubit gate scheme and characterize gate performance metrics within our scalable cluster-based qubit scheme. Since the scheme incorporates both NMR and ESR operations, we use the Toffoli gate as a representative multi-qubit gate. We take the 2P-3P cluster pair as an example, as shown in Fig. 2(c). The HF interaction strengths in the cluster pair are given by $[A_{1L}, A_{2L}, A_{1R}, A_{2R}, A_{3R}]$ =[60, 170, A_0 , 120, 230] MHz. In this section, errors induced by crosstalk and single-qubit decoherence

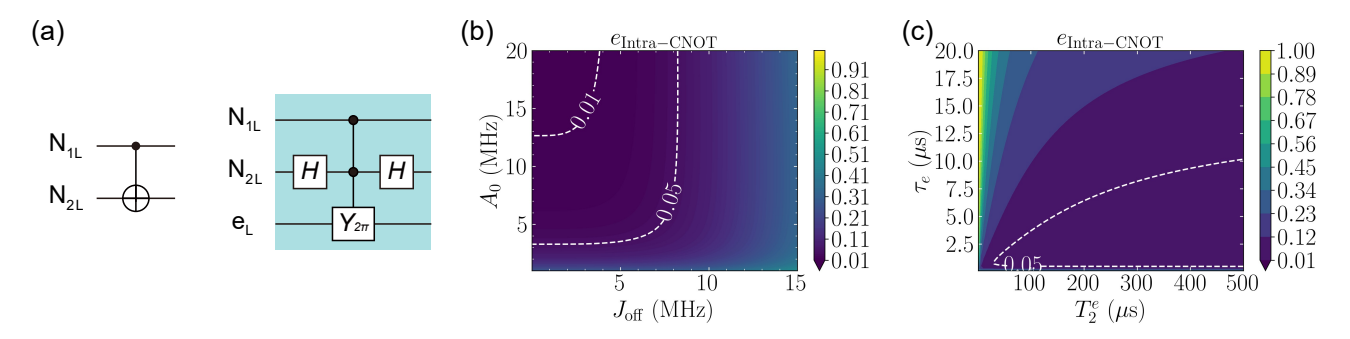


FIG. 5. Intra-cluster CNOT-type gate between nuclear spin qubits. (a) The intra-cluster CNOT gate with N_{1L} as the control qubit and N_{2L} as the target qubit and its compiled circuit. The CNOT gate is composed of an ESR-based CZ gate and two single-qubit gates applied to N_{2L} . (b) The infidelity $e_{\text{Intra}-\text{CNOT}}$ of the intra-cluster CNOT-type gate is plotted as a function of the residual exchange interaction J_{off} and the hyperfine interaction A_0 . (c) The infidelity $e_{\text{Intra}-\text{CNOT}}$ of the intra-cluster CNOT-type gate is plotted as a function of the decoherence time T_2^e and the 2π -rotation time τ_e of the electron spin.

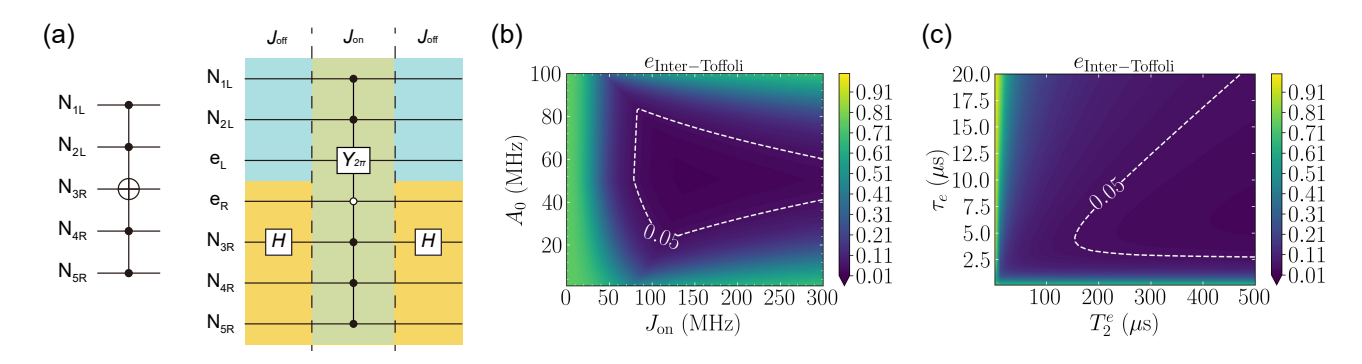


FIG. 6. Inter-cluster Toffoli-type gate between nuclear spin qubits. (a) The inter-cluster five-qubit Toffoli gate with N_{3R} as the target qubit and the other four nuclear spins as control qubits, along with its compiled circuit. The Toffoli gate is composed of an ESR-based inter-cluster CCCCZ gate and two single-qubit gates applied to N_{3R} . (b) The infidelity $e_{\text{Inter-Toffoli}}$ of the inter-cluster Toffoli-type gate is plotted as a function of the activated exchange interaction J_{on} and the hyperfine interaction A_0 . (c) The infidelity $e_{\text{Inter-Toffoli}}$ of the inter-cluster Toffoli-type gate is plotted as a function of the decoherence time T_2^e and the 2π -rotation time τ_e of the electron spin.

are considered (see the Supplementary Material for details). The dephasing time of the nuclear spin is set to 40 ms [15]. The strength of the time-dependent drive for NMR operations is assumed to be 1 mT. Then, the NMR operation time depends on the corresponding HF interaction strength. Since the electron spin only undergoes 2π rotation operations, we set the electron spin decoherence time to 400 μ s, corresponding to the typical spin-echo dephasing time [3]. The Rabi frequency of intra-cluster ESR operations is assumed to be 0.5 MHz, while that of inter-cluster ESR operations is 0.3 MHz.

The compiled circuit for a nuclear-nuclear CNOT gate within the 2P cluster (with $\rm N_{2L}$ as the target qubit) is shown in Fig. 5(a). The CNOT gate is realized by applying Hadamard H gates to the target nuclear spin qubit before and after the CZ gate. To give a conservative performance estimate, we calculate the infidelity of CNOT gates with the most severe crosstalk in the ESR operations. In Fig. 5(b), the dependence of the CNOT gate infidelity $e_{ct}^{\rm Intra-ESR}$ on $J_{\rm off}$ and ΔA is similar to that

of intra-cluster ESR operations. The effect of single-qubit decoherence is shown in Fig. 5(c), where $J_{\rm off}=3$ MHz and $A_0=15$ MHz. The selectable electron manipulation time can be determined by the region enclosed by the white dashed lines, corresponding an infidelity of $e_{\rm Intra-Toffoli}<0.05$). The upper bound of the ESR operation time τ_e is determined by the electron decoherence time T_2^e , while the lower bound is limited by the minimum frequency detuning required to avoid driving errors. The trade-off between crosstalk error and decoherence-induced error can be mitigated by optimizing the coherence of qubits.

The compiled circuit for a five-qubit Toffoli gate between the 2P and 3P clusters with N_{3R} as the target qubit, is shown in Fig. 6(a). Similarly, to assess the performance in the worst case, only the multi-qubit CC-CCZ gate with the minimum difference between ESR frequencies is considered, and the infidelity $e_{\rm Inter-Toffoli}$ of the inter-cluster Toffoli-type gate is calculated, as shown in Fig. 6(b). A region with low infidelity (< 0.05) is achieved for HF strength ranging from 30 MHz to

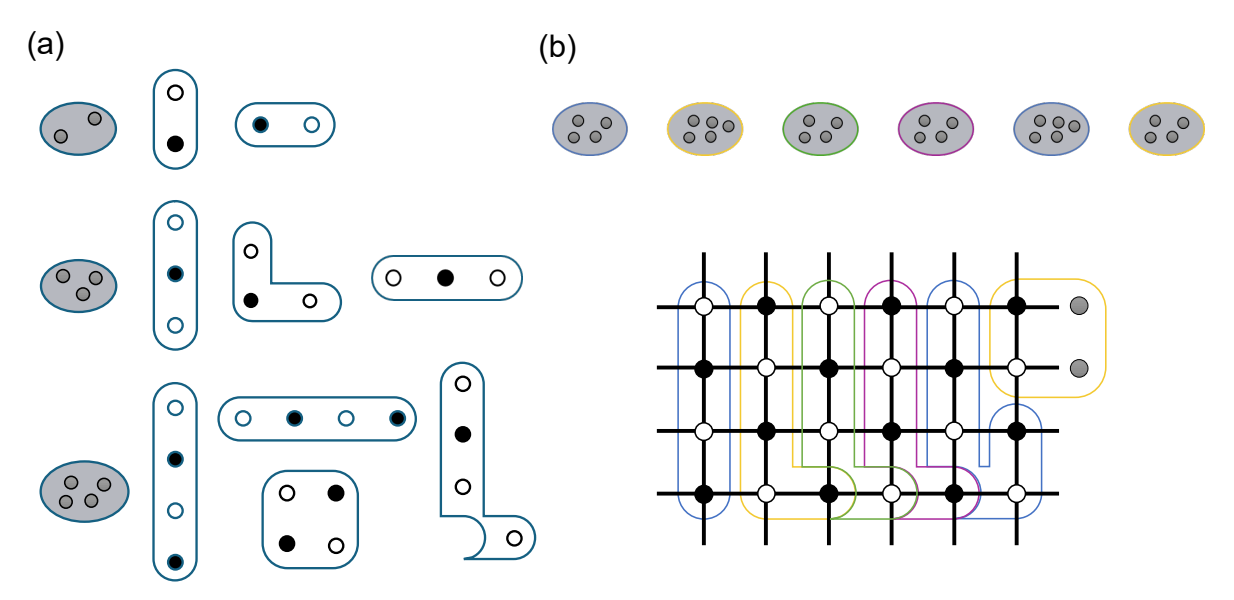


FIG. 7. Quantum error correction in cluster-based qubit systems. Gray dots represent nuclear spin qubits within clusters. White dots indicate data qubits, while black dots represent ancillary qubits. (a) The mapping between clusters and parts of the 2D toric code is shown. The shape of the mapped modules constructed by qubits within a cluster can be modified arbitrarily due to the all-to-all connectivity among them. (b) A 2D [[12,2,3]] XZZX toric code is constructed using a 1D cluster chain. Vertical lines represent Z-type Pauli checks, while horizontal lines indicate X-type Pauli checks.

90 MHz. The optimal exchange interaction strength is stronger than 80 MHz. In Fig. 6(c), the infidelity $e_{\rm Inter-Toffoli}$ is plotted as a function of the decoherence time T_2^e and the operation time τ_e of the electron spin. Compared to the results of intra-cluster CNOT gates, achieving a low infidelity (< 0.05) requires a longer T_2^e and permits a shorter feasible range of τ_e . This is primarily because crosstalk errors are more severe when performing inter-cluster Toffoli gates, further emphasizing the importance of crosstalk suppression.

IV. DISCUSSION AND OUTLOOK

There are several interesting features of our proposed cluster-based quantum computing architecture. First, certain randomness in both the position and the number of donors within each cluster is acceptable, which reduces the challenges associated with the deterministic placement of donors and thereby facilitates the fabrication process. Moreover, inherent randomness in the HF interaction strengths of donors results in a frequency distribution of spin qubits, which suppresses crosstalk errors and enables the addressability of the donor nuclear spins. Therefore, this donor cluster-based architecture harnesses rather than eliminates fabrication randomness.

Moreover, this cluster-based spin qubit scheme also demonstrates unique advantages for quantum error correction codes, owing to its local all-to-all-connected topology and low-overhead multi-qubit gates. In stabilizer codes, the most essential operation is stabilizer measurement, which is typically implemented using CNOT gates between ancillary qubits and data qubits. In the

cluster-based system, the combination of multi-qubit CZ gates and single-qubit operations enables the realization of a CXX gate, which acts on one control and multiple target qubits. The CXX gate can perform the same function as two CNOT gates, with reduced operation time.

The features of cluster spin qubits can be applied to optimize implementation of surface codes. For instance, when implementing surface codes, each cluster serves as a reconfigurable module. As illustrated in Fig. 7, a 4Pcluster can be arranged into various configurations, including horizontal chain, vertical chain, square lattice, and other topological arrangements. This characteristic not only ensures the flexible implementation of topological codes but also enables the construction of topological codes with higher effective dimensions than those of the physical architecture. For example, as shown in Fig. 7(b), a 1D cluster chain can be projected to form a 2D [[12,2,3]] XZZX toric code [26], an error-correcting code specifically designed for biased noise. While the cluster architecture only permits limited expansion along one additional physical dimension, this constraint naturally aligns with the requirements of bias-tailored codes. Notably, silicon-based spin qubit systems inherently exhibit such noise bias characteristics, with the gubit relaxation time significantly longer the dephasing time. With such highly biased noise, the fidelity threshold for fault tolerance can be significantly lowered [25]. However, the practical performance of the XZZX code applied in the cluster-based scheme depends on the specific device. Further detailed QEC scheme and evaluation of error correction performance are subjects for future research.

Furthermore, for 2D cluster arrays, QEC codes could also be extended to high-dimensional codes [38–40]. De-

signing and optimizing QEC schemes specifically adapted to a 2D cluster array represents a valuable direction for further research. Considering the local all-to-all connectivity of qubits, the cluster architecture is also highly compatible with low-density parity-check (LDPC) codes [26, 38, 41], qLDPC codes have demonstrated the capability to substantially reduce the physical resource overhead required for quantum error correction [26, 38, 41]. The qLDPC scheme based on a scalable cluster-based architecture represents another promising avenue for scalable fault tolerance.

To achieve fault-tolerant quantum computation (FTQC) encoding within the proposed architecture, several critical technologies require further development [42, 43]. First, enhanced tunability is needed for precision control of both HF interaction and exchange interaction, to enable high-fidelity gate operations. The fast and high-fidelity QND readout of nuclear spins within clusters must be realized, as it provides a critical foundation for mid-circuit measurement capabilities [44, 45], enabling real-time syndrome extraction and feedback control without disturbing the subsequent operations. Moreover, noise-mitigation techniques, such as dynamical decoupling and pulse optimization, should be integrated to suppress the error rate of qubit operations. These advancements will bridge the gap between the current state of cluster arrays and a fully functional FTQC platform.

While our proposed scheme addresses the issue of frequency crowding and enables scalability of the array, qubit scaling within a single cluster array remains limited. Given the state-of-the-art magnetic field gradient ($\approx 0.2 \text{ mT/nm}$ [46]) provided by the micromagnets and the bandwidth constraints of a single microwave antenna, the practical number of qubits addressable in a single array is limited to the order of hundreds. To further enhance scalability, one approach is to interconnect distant cluster arrays, potentially utilizing shuttling techniques with moving quantum dots [47–52] or cQED cavities [53–56]. Alternatively, local electrical manipulation schemes, such as electrical-dipole spin resonance (EDSR) [18, 57, 58] or baseband hopping control [12, 59], could be employed to circumvent the frequency crowding issue. These strategies offer promising pathways for increasing the total number of integrated qubits.

The cluster structure demonstrates unique advantages within phosphorus-donor nuclear spin systems. In the future, this architecture can also be adapted to other dopant species. For example, acceptor atoms such as boron or aluminum feature bound holes that permit fast electrical dipole spin resonance (EDSR) control [60, 61]. Additionally, high-spin nuclei, such as antimony, arsenic, and aluminum, enable qudit [62] and logical qubit encodings [63]. Extending the cluster paradigm to these systems is highly promising, as it could leverage their respective advantages to enhance processor capabilities for large-scale quantum computation in silicon.

V. CONCLUSION

In this work, we propose a scalable spin qubit scheme based on donor cluster arrays. By utilizing electron spins as ancillas, addressable single-qubit operations on nuclear spin gubits can be achieved, along with intra- and inter-cluster multi-qubit gates. The incorporation of tunable exchange interactions and micromagnets provides a viable solution to the potential bottleneck of frequency crowding. Furthermore, through the strategic design of ESR- and NMR-assisted qubit operations, crosstalk errors can be effectively suppressed. Our calculations quantify the impact of HF coupling, exchange interaction and magnetic field gradients on qubit gate fidelity, establishing experimental parameter requirements. To leverage the advantages of this scalable architecture, we propose viable QEC schemes tailored to the unique characteristics of cluster-based spin-qubit systems. In conclusion, our proposed scalable spin qubit scheme establishes a solid theoretical foundation for the further development of silicon-based spin qubits and provides a viable pathway toward the realization of large-scale quantum processors.

ACKNOWLEDGMENTS

This work was supported by the National Natural Science Foundation of China.

SUPPLEMENTARY MATERIAL

Appendix A: Scalable cluster-based qubit scheme with tunable couplers

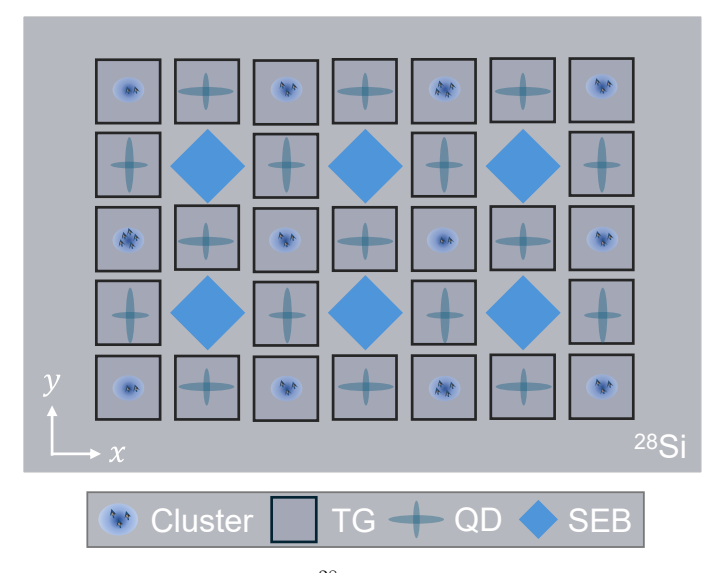


FIG. 1. Scalable cluster-based spin qubit scheme in ²⁸Si. (a) Donor clusters are arranged into a two-dimensional array. Each donor cluster contains multiple P donors and one electron bound to them. To achieve tunability of exchange interactions between neighboring electrons, the inter-cluster units are quantum dot (QDs) to induce tunable superexchange interactions. Top gates (TGs) above clusters are used to adjusting energy detuning between clusters. The inter-cluster units could be quantum dots (QDs) or TG to adjust tunneling between clusters. Additionally, single-lead quantum dots are incorporated between clusters for readout and loading of electrons.

In our proposed scheme of the main text, tunable exchange coupling is achieved via top gates. An alternative coupler is a gate-defined quantum dot (QD). With the mediation of the QD, a 'superexchange' coupling can be induced between electron spins in adjacent clusters [28, 30, 64, 65]. The strength of the superexchange coupling between two electrons can be expressed as

$$J_{\rm SE} = t_{c1}^2 t_{c2}^2 \beta(\epsilon_1 \epsilon_2),\tag{A1}$$

where t_{c1} (t_{c2}) is the tunneling between the first (second) cluster and the middle QD. β is a function of the detuning ϵ_1 (ϵ_2) between the first (second) cluster and the QD. By adjusting detunings, the strength $J_{\rm SE}$ is highly tunable. Consequently, the superexchange coupling can be effectively suppressed, which is crucial for crosstalk mitigation. Moreover, the shape of QD can be engineered to capture better control capability.

Appendix B: Scalable cluster-based qubit scheme under state-of-the-art techniques

Indeed, to realize a fully scalable 2D architecture, several experimental techniques still require verification and breakthroughs, such as top-gate control, mid-circuit readout, and narrow gates. Nevertheless, the implementation of 1D cluster chains remains feasible. Moreover, owing to the local all-to-all connectivity within cluster systems, even 1D chains can demonstrate advanced error-correction codes like the XZZX surface code. Fig. 2 illustrates the spin-qubit device based on a 1D cluster chain achievable with state-of-the-art technologies. In the architecture, in-plane gates are distributed on opposite sides of the chain to minimize crosstalk, and are utilized to adjust the electrochemical potentials of both the clusters and SLQDs. Readout and initialization of qubits can be achieved with mediation of electrons and SLQDs. Additionally, a micromagnet is incorporated to generate the required magnetic field gradient. The 1D cluster architecture not only provides sufficient qubits for near-term demonstration applications but also establishes the technical foundation and feasibility proof for future 2D scalable implementations.

In the state-of-the-art device, the exchange interaction is switched by adjusting the energy detuning between clusters. In this way, when the exchange interaction is turned on, the effect of charge noise on the exchange interaction is enhanced. Consequently, the fidelities of the inter-cluster qubit operations are reduced. We calculate the infidelities of the intra-cluster CNOT gate and inter-cluster Toffoli gate in a 2P-3P cluster system, same with the main text.

Here, the noise-induced exchange interaction variation is considered. The tunneling rate between clusters is set to 3.6 GHz. The Coulomb potential U is 30 meV. The corresponding exchange coupling at the charge symmetry point is approximately 7 MHz. As shown in Fig. 2(b), the infidelity of the intra-cluster CNOT gate is similar with that without considering exchange variation (Fig. 5(b) in the main text). This is because the sensitivity of the exchange interaction on charge noise is suppressed around the charge symmetry point. However, as shown in Fig. 2(c), the fidelity of the inter-cluster Toffoli gate is significantly reduced compared to Fig 6(b) in the main text. Moreover, the selectable range of both the exchange interaction coupling and the HF difference is reduced, which imposes more stringent requirements on the device fabrication. The using of the top gate or superexchange is essential for the scaling-up of the cluster-based system.

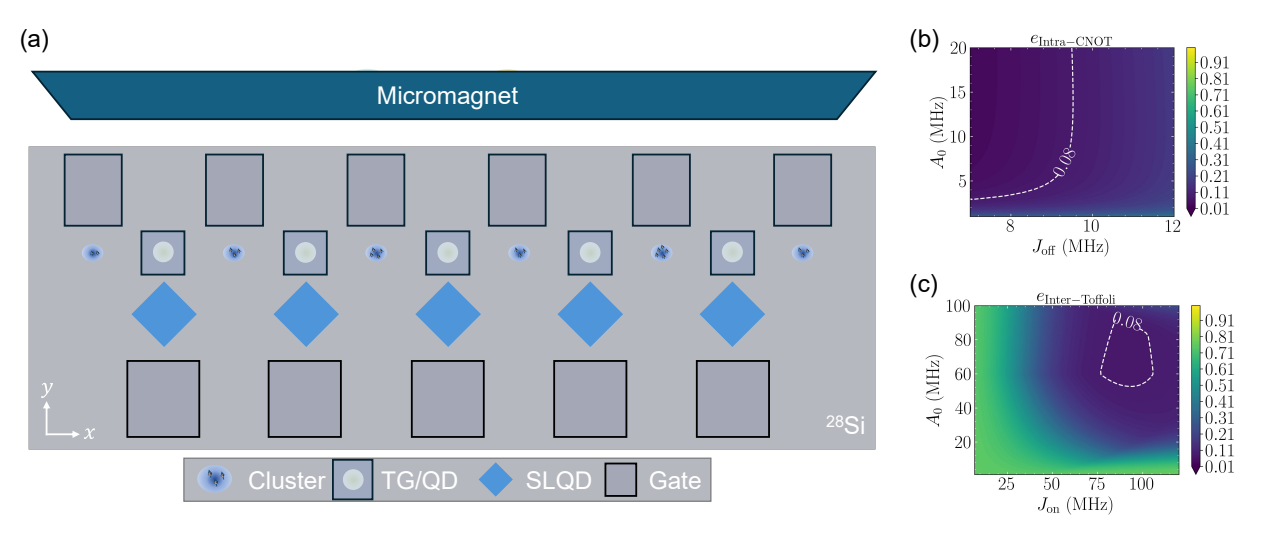


FIG. 2. Scalable cluster-based spin qubit scheme in 28 Si. Donor clusters are arranged into a one-dimensional chain. Each donor cluster contains 2-4 P donors and one electron bound to them. To achieve tunability of exchange interactions between neighboring electrons, the inter-cluster units can be implemented either as top gates (TGs) for adjusting tunneling or as quantum dot (QDs) to induce tunable superexchange interactions. Additionally, single-lead quantum dots (SLQDs) are incorporated between clusters for readout and loading of electrons. The control gates for the clusters and the SLQDs are arranged on opposite sides (upper and lower) of the cluster chain. Moreover, a micromagnet is positioned adjacent to the cluster chain to generate magnetic field gradients, which mitigate the frequency crowding issue. (b) The infidelity $e_{\text{Intra}-\text{CNOT}}$ of the intra-cluster CNOT-type gate is plotted as a function of the residual exchange interaction J_{off} and the hyperfine interaction J_{on} and J_{on} a

Appendix C: Optimized donor number within a single cluster

Stochastic placement of donors can lead to randomness in the numbers of donors within each cluster. However, variation in the number of donors within a cluster is acceptable for a cluster-based qubit system. When the number of donors in the cluster unexpectedly increases, the excess nuclear spins can be excluded from the qubit set after they are initialized. A decrease in the number of donors does not disrupt the cluster array structure, as the nuclear spin qubits within the array remain interconnected via exchange interactions. Although variation in the number of donors does not affect the feasibility of the cluster-based scheme, determining the optimal range of donor numbers can ensure good operation performance of the qubits. If there are too few donors within a cluster, more inter-cluster operations will be required, reducing the overall operational precision. In contrast, if there are too many donors in a cluster, the local CNOT gate cost within the cluster will increase significantly. This is because conditional ESR pulses must be applied more extensively to account for all possible states, effectively shielding the influence of other nuclei. Additionally, since the HF coupling strength depends on the overlap between the corresponding nuclear and electron wavefunctions, an large number of donors can lead to similar HF strength among nuclei within the cluster. This results in frequency crowding, making individual addressing more challenging due to overlapping resonance frequencies.

To estimate the upper bound of donor numbers within a single cluster, we performed numerical simulations to model the HF strength distribution within a single cluster. Considering an ESR Rabi frequency of 0.5 MHz, a frequency difference of 5 MHz is required to ensure the crosstalk error below 1%. We randomly sampled HF couplings from the experimentally reported range of 0.6 MHz to 304 MHz until the difference between any two HF strengths was less

than 10 MHz. By 1000 samplings, the feasible number of donors within a cluster ranges from 2 to 11. The average number is 4.3 (1.5). With crosstalk mitigation techniques or slower ESR driving, the feasible number of donors within a cluster can be further increased.

Appendix D: Analytical calculation

Analytical calculations help better understand the impact of different interactions on qubit operations, particularly the crosstalk issue when frequency detuning is insufficient. We consider cluster with $N_{\rm L}$ donors and a neighboring cluster with $N_{\rm R}$ donors, whose Hamiltonian can be expressed as

$$H_{2C,0} = B_0 \left[\sum_{i}^{L,R} \gamma_e S_z^i + \sum_{i=1}^{N_L + N_R} \gamma_n S_z^i \right] + \sum_{i=1}^{N_L} A_i \mathbf{S_L} \cdot \mathbf{I^i} + \sum_{i=N_L + 1}^{N_L + N_R} A_i \mathbf{S_R} \cdot \mathbf{I^i} + J \mathbf{S_L} \cdot \mathbf{S_R}.$$
(D1)

where γ_e and γ_n are the gyromagnetic ratio for the electron spin and the nuclear spin, $A_i^{\mathrm{L(R)}}$ is the strength of the hyperfine interaction between electron spin and nuclear spins on the left (right) donor, and J is the exchange coupling between electron spins. $\mathbf{S_{L(R)}}$ is the spin operator for the left (right) electron spin. $\mathbf{I^i}$ is the spin operator for the left (right) nuclear spin of nucleus i. The system Hamiltonian includes Zeeman terms, HF terms and exchange terms. By diagonalizing H_{2C} , the energies of electron spin states with different combination of nuclear spin states can be obtained:

$$E_{\downarrow_{L}\downarrow_{R},\{n_{i}\}} = -\gamma_{e}B_{0} + \sum_{i=1}^{N_{L}+N_{R}} (-1)^{m_{i}} \frac{\gamma_{n}B_{0}}{2} - \sum_{i=1}^{N_{L}} (-1)^{m_{i}} \frac{A_{i}}{4} - \sum_{i=N_{L}+1}^{N_{L}+N_{R}} (-1)^{m_{i}} \frac{A_{i}}{4} + \frac{J}{4},$$

$$E_{\downarrow_{L}\uparrow_{R},\{n_{i}\}} = \sum_{i=1}^{N_{L}+N_{R}} (-1)^{m_{i}} \frac{\gamma_{n}B_{0}}{2} \mp \frac{\sqrt{\Delta^{2}(A_{i})+4J^{2}}}{4} - \frac{J}{4},$$

$$E_{\uparrow_{L}\downarrow_{R},\{n_{i}\}} = \sum_{i=1}^{N_{L}+N_{R}} (-1)^{m_{i}} \frac{\gamma_{n}B_{0}}{2} \pm \frac{\sqrt{\Delta^{2}(A_{i})+4J^{2}}}{4} - \frac{J}{4},$$

$$E_{\uparrow_{L}\uparrow_{R},\{n_{i}\}} = \gamma_{e}B_{0} + \sum_{i=1}^{N_{L}+N_{R}} (-1)^{m_{i}} \frac{\gamma_{n}B_{0}}{2} + \sum_{i=N_{L}+1}^{N_{L}+N_{R}} (-1)^{m_{i}} \frac{A_{i}}{4} + \sum_{i=1}^{N_{L}} (-1)^{m_{i}} \frac{A_{i}}{4} + \frac{J}{4},$$

$$(D2)$$

where n_i represents different combinations of nuclear spins, determining the value of m_i . When the nuclear spin state n_i is $|\uparrow\rangle$ ($|\downarrow\rangle$), $m_i = 0$ (1). Additionally,

$$\Delta(A_i) = ((-1)^{n_L} \sum_{i=1}^{N_L} (-1)^{m_i} A_i + (-1)^{n_R} \sum_{i=N_L+1}^{N_L+N_R} (-1)^{m_i} A_i).$$
 (D3)

Notably, $n_{\rm L}$ and $n_{\rm R}$ represent states of left and right electron spin respectively. $n_i = 0$ (1) for the electron spin state $|\uparrow\rangle$ ($|\downarrow\rangle$). For the cluster-based scheme, since state of electron spin is fixed to $|\downarrow\rangle$ state, the NMR frequency for the *i*-th nuclear spin is

$$\hbar\omega_i = |\gamma_n B_0 + \frac{A_i}{2}|. \tag{D4}$$

The ESR frequencies for both electron spins can be calculated:

$$\hbar\omega_{\uparrow_{L}\downarrow_{R},\{n_{i}\}} = \gamma_{e}B_{0} + \sum_{i=1}^{N_{L}+N_{R}} (-1)^{m_{i}} \frac{A_{i}}{4} - \frac{J}{2} \pm \frac{\sqrt{\Delta^{2}(A_{i}) + 4J^{2}}}{4},$$

$$\hbar\omega_{\uparrow_{L}\uparrow_{R},\{n_{i}\}} = \gamma_{e}B_{0} + \sum_{i=1}^{N_{L}+N_{R}} (-1)^{m_{i}} \frac{A_{i}}{4} + \frac{J}{2} \pm \frac{\sqrt{\Delta^{2}(A_{i}) + 4J^{2}}}{4},$$

$$\hbar\omega_{\downarrow_{L}\uparrow_{R},\{n_{i}\}} = \gamma_{e}B_{0} + \sum_{i=1}^{N_{L}+N_{R}} (-1)^{m_{i}} \frac{A_{i}}{4} - \frac{J}{2} \mp \frac{\sqrt{\Delta^{2}(A_{i}) + 4J^{2}}}{4},$$

$$\hbar\omega_{\uparrow_{L}\uparrow_{R},\{n_{i}\}} = \gamma_{e}B_{0} + \sum_{i=1}^{N_{L}+N_{R}} (-1)^{m_{i}} \frac{A_{i}}{4} + \frac{J}{2} \mp \frac{\sqrt{\Delta^{2}(A_{i}) + 4J^{2}}}{4},$$

$$\hbar\omega_{\uparrow_{L}\uparrow_{R},\{n_{i}\}} = \gamma_{e}B_{0} + \sum_{i=1}^{N_{L}+N_{R}} (-1)^{m_{i}} \frac{A_{i}}{4} + \frac{J}{2} \mp \frac{\sqrt{\Delta^{2}(A_{i}) + 4J^{2}}}{4},$$

where $\hbar\omega_{\uparrow_i\downarrow_j}$ ($\hbar\omega_{\uparrow_i\uparrow_j}$) represents the ESR frequency of the electron i when the electron j is in the spin-down (up) state. Using Eq. (D5), the conditional ESR frequencies can be calculated for different control configurations. Then, the minimum frequency difference can be obtained to estimate the crosstalk error on ESR-based multi-qubit CZ gate under specific parameters.

Appendix E: Numerical calculation

In this work, numerical calculations are perform by solving the Schrödinger equation:

$$i\hbar \frac{\partial}{\partial t} \mid \psi(t) \rangle = H(t) \mid \psi(t) \rangle,$$
 (E1)

where H(t) is the time-dependent Hamiltonian for the clusters. Here, H(t) is obtained by expressing the system Hamiltonian in a proper rotating frame. In this work, the rotating frame is defined with respect to the diagonalized static Hamiltonian. In such rotating frame, the resonant driving terms become time-independent:

$$d_{ij} = d_0, (E2)$$

where d_0 is the effective strength of driving between state i and state j. The off-resonant terms remain oscillatory:

$$d_{i'j'} = d_0' e^{\pm i\Delta' t}, \tag{E3}$$

where $\Delta' = \hbar \omega_{ij} - \hbar \omega_{i'j'}$ is the frequency detuning. Thus, the crosstalk issue caused by frequency crowding can be effectively captured.

Next, to investigate the impact of noise on qubit operations, we also incorporated noise simulation. In silicon-based spin qubit systems, qubit dephasing is the dominant decoherence process, typically caused by 1/f noise in 28 Si. The 1/f noise sequence generation follows the approach described in Ref. []. The 1/f noise generation process os as follows: First, a time-domain Gaussian white noise sequence $\{\delta_i\}$ is generated via a randomization procedure. Then, the noise sequence is transformed into the frequency domain via Fourier transform. Next, the noise intensity is scaled by multiplying it with a frequency-dependent scaling factor $S_n = c_\varepsilon^2 N/(n-1)$, where N is the total numbers of elements in the sequence. Finally, the frequency domain noise is converted back to the time domain through an inverse Fourier transform, resulting in the 1/f noise sequence $\{\delta_i^{1/f}\}$. For spin qubit j, the noise-induced qubit frequency shift at time point i is given by

$$\delta\hbar\omega_j = \varepsilon_j \delta_i^{1/f}. \tag{E4}$$

Then, the noise-induced effects are then incorporated by adding the detuning Hamiltonians of spin qubits:

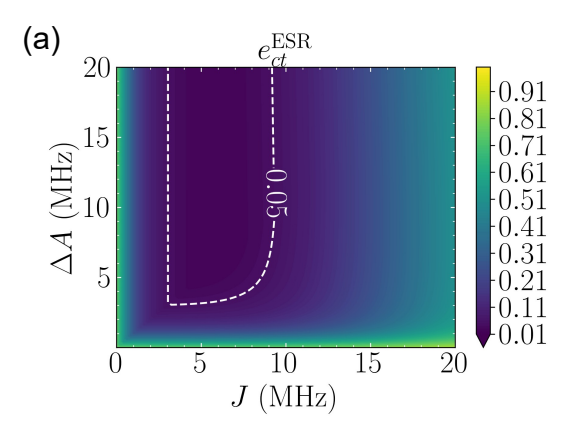
$$H_{\delta,j} = \delta \hbar \omega_j \frac{\sigma_{Z,j}}{2},\tag{E5}$$

where the Pauli-Z matrix is corresponding to spin qubit j.

Appendix F: Comparison between direct and NMR/ESR-assisted inter-cluster CZ gate

Although our proposed scheme can reduce the possibility of frequency crowding, it may still arise during large-scale qubit expansion, leading to crosstalk. For the intra-cluster operations, crosstalk mitigation techniques on control can suppress the errors. However, for the inter-cluster nuclear-nuclear CZ gates, the frequency crowding issue becomes more severe. To avoid the crosstalk, a compromise solution is to implement inter-cluster CZ gates indirectly. There are two alternative approach for indirect nuclear-nuclear multi-qubit gates. A 2P-3P cluster pair serves as an example to illustrate the two approach.

The first approach is assisted by ESR operations. For example, the target operation is a CCCCZ-like gate on N_1 for the combined states of other nuclear spin is $|\psi_2\psi_3\psi_4\uparrow_5\rangle$, which may be difficult to be implemented directly due to frequency crowding. This can be addressed by first applying a conditional π -operation on the right electron for the nuclear spin state $|\psi_3\psi_4\uparrow_5\rangle$ within right clusters, thereby transferring the condition on nuclear spins to the electron spin. Subsequently, a 2π rotation on the left electron spin is applied conditional on the state $|\psi_1\psi_2\uparrow_R\rangle$, effectively realizing the target CCCCZ-like gate. Finally, the entire target operation is completed by rotating the right electron spin back to the spin-down state.



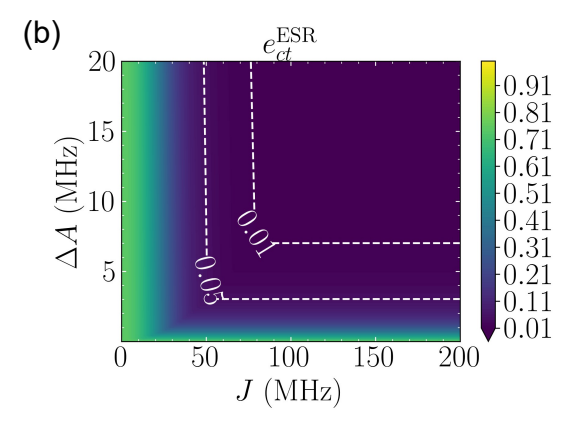


FIG. 3. Addressability of ESR-assisted and NMR-assisted inter-cluster ESR operations. (a) Crosstalk error $e_{ct}^{\rm ESR}$ for the ESR-assisted CZ gate is plotted as a function exchange interaction J and the minimum difference between HF coupling strengths ΔA . (b) Crosstalk error $e_{ct}^{\rm ESR}$ for the NMR-assisted CZ gate is plotted as a function exchange interaction J and the minimum difference between HF coupling strengths ΔA .

The second approach is assisted by NMR operations. Typically, the ESR frequencies controlled by the all-up and all-down nuclear spin states can be addressed relatively well. Therefore, we can combine NMR π -rotations and the multi-qubit CZ gate conditioned on the all-up (all-down) state to implement the target multi-qubit CZ gate. We again use the CZ gate as a target operation to illustrate this approach. $|\psi_1\psi_2\psi_3\psi_4\uparrow_5\rangle$ state can be transformed into the all-down state $(|\psi_1\psi_2\psi_3\psi_4\psi_5\rangle)$ with fewer NMR operations than into the all-up state. Thus, a NMR π -rotation is applied to the qubit N₅. Then, the ESR 2π -rotation controlled by the all-down nuclear spin states is applied. Finally, an inverse NMR π -rotation is applied to the qubit rmN_5 , effectively achieving the target nuclear-nuclear CZ gate.

Both approaches can effectively mitigate the crosstalk errors caused by frequency crowding. When implementing an mCZ gate (m is the number of involved qubits), the ESR-assisted approach requires 2^{a-1} additional ESR operations compared to direct implementation. a is the smallest numbers of nuclei within a cluster. In contrast, the NMR-assisted approach requires 2^{b-2} additional NMR operations compared to direct implementation. b is the number of nuclei within the two adjacent clusters. The ESR-assisted approach typically requires fewer additional operations compared with NMR-assisted approach. Considering the faster ESR operation speed, this approach results in a relatively low circuit depth. However, when turning on the exchange interaction J to implement the CNOT gate between electron spins, the driving strength must be sufficiently strong to avoid being affected by the nuclear spin states in the adjacent cluster. Unfortunately, such strong ESR driving can easily induce crosstalk errors, especially in a large-scale qubit system. The NMR-assisted approach offers the advantage of higher operational precision and is less likely to introduce additional crosstalks. However, this approach requires longer operations time, when the control state (corresponding to the target operation) is far from both the all-up and all-down nuclear spin states. In summary, both schemes have their own advantages and disadvantages. Therefore, the choice between the two approaches should be determined based on the specific practical situation.

We calculated the cross-talk errors $e_{ct}^{\rm ESR}$ for both the ESR-assisted and NMR-assisted inter-cluster ESR operation. The result for ESR-assisted scheme is shown in Fig. 3(a). In this scheme, the desirable strength of the exchange interaction is approximately from 3 to 10 MHz. This is because nuclear spin qubits within adjacent clusters are no longer required to serve as control qubits. Instead, the dependence on them of ESR operations should be suppressed. The exchange interaction must be neither too strong nor too weak. As shown in Fig. 3, an exchange interaction stronger than 50 MHz is sufficient. For the NMR-assisted scheme, only address the ESR on a single nuclear spin state is required. Therefore, the frequency difference increases monotonically with the enhancement of both the exchange interaction and the HF difference, thus reducing crosstalk errors. Both of the scheme, the requirement for HF difference is stringent. These two schemes serve as optional complements for control protocol for the cluster-based qubit scheme, and can be selectively employed based on the specific ESR frequency distribution within the device and the particular circuit design.

Appendix G: Error model

This section describes the error models considered in the work and their corresponding calculations. There are three kinds of error sources: qubit decoherence, noise-induced exchange interaction variation, and crosstalk.

Assuming the decoherence time of the nuclear spin qubit is $T_{2,n}$, the error induced by nuclear spin decoherence during the operation time τ of the whole circuit can be approximated by

$$e_{T_{2,n}} = 1 - e^{-\frac{\tau}{T_{2,n}}}.$$
 (G1)

Since electron spin qubits have long relaxation times and are only used as ancilla qubits, only the electron spin decoherence during the ESR-based CZ gate is considered. The corresponding error is represented by

$$e_{T_{2,e}} = 1 - e^{-\frac{\tau_{\rm ESR}}{T_{2,e}}},$$
 (G2)

where $\tau_{\rm ESR}$ is the operation time of 2π ESR operations, and $T_{2,e}$ is the decoherence time of electron spin qubit. Charge noise leads to variations in the exchange interaction. The exchange interaction is expressed as

$$J = \frac{4t_c^2 U}{U^2 - \epsilon^2},\tag{G3}$$

where t_c is the tunneling between clusters, U is the on-site Coulomb interaction, ϵ is the energy detuning of the electron between clusters. To estimate the variation due to charge noise, the first derivative of J with respect to ϵ yields

$$\frac{\partial J}{\partial \epsilon} = \frac{8t_c^2 U \epsilon}{(U^{2-\epsilon^2})^2}.$$
 (G4)

Then, then variation in J is

$$\delta J = \delta \epsilon \frac{\partial J}{\partial \epsilon},\tag{G5}$$

where $\delta\epsilon$ is the variation in the ϵ . Then, δJ is taken into the total energy variation $\epsilon\varepsilon$ to obtain the modified decoherence time $T_{2,e}^{\delta J}$.

Due to the frequency crowding issue, crosstalk errors may arise during the driving. Assuming a frequency detuning $\Delta\hbar\omega$ and resonant driving strength f, the crosstalk error can be estimated as

$$e_{ct} = \frac{f^2}{f^2 + (\Delta\hbar\omega)^2}.$$
(G6)

The frequency detuning is calculated by analytical results described in Sec. D. This equation can also be used to estimate the driving error when there is detuning $\Delta\hbar\omega_1$ between the driving frequency and the target frequency:

$$e_{detuning} = 1 - \frac{f^2}{f^2 + (\Delta\hbar\omega_1)^2}.$$
 (G7)

The detuning error is considered when calculating fidelities of intra-cluster multi-qubit gates with the residual exchange interaction J_{off} . When considering crosstalk error in ESR-based CZ gates, Eq. (G6) is modified to more accurately estimate the error on the nuclear spin qubits:

$$e_{ct}^{\text{ESR}} = 1 - \frac{1}{4} \left[1 + \sqrt{1 - \frac{f^2}{f^2 + (\Delta\hbar\omega)^2}} \right]^2.$$
 (G8)

However, it should be noted that the crosstalk error estimated by the equation remains larger than the practical situation.

Using the methods for error calculation, fidelities of quantum gates can be calculated accordingly. For example, a intra-cluster three-qubit Toffoli gate for a 3P cluster includes two NMR pulses and one ESR pulse. The fidelity can be obtained by

$$F_{\text{Intra-Toffoli}} = (1 - e_{T_{2,n}})(1 - e_{T_{2,e}}^{\delta J})(1 - e_{ct})(1 - e_{detuning}).$$
 (G9)

Similarly, the fidelity of a CNOT gate including two NMR pulses and two ESR pulses is

$$F_{\text{Intra-Toffoli}} = (1 - e_{T_{2,n}})(1 - e_{T_{2,e}}^{\delta J})^2 (1 - e_{ct})^2 (1 - e_{detuning})^2.$$
 (G10)

[1] B. E. Kane, A silicon-based nuclear spin quantum com-[2] D. Loss and D. P. DiVincenzo, Quantum computation puter, Nature **393**, 133 (1998).

- with quantum dots, Phys. Rev. A 57, 120 (1998).
- [3] A. M. Tyryshkin, S. Tojo, J. J. Morton, H. Riemann, N. V. Abrosimov, P. Becker, H.-J. Pohl, T. Schenkel, M. L. Thewalt, K. M. Itoh, et al., Electron spin coherence exceeding seconds in high-purity silicon, Nat. Mater. 11, 143 (2012).
- [4] K. Saeedi, S. Simmons, J. Z. Salvail, P. Dluhy, H. Riemann, N. V. Abrosimov, P. Becker, H.-J. Pohl, J. J. L. Morton, and M. L. W. Thewalt, Room-temperature quantum bit storage exceeding 39 minutes using ionized donors in silicon-28, Science 342, 830 (2013).
- [5] J. T. Muhonen, J. P. Dehollain, A. Laucht, F. E. Hudson, R. Kalra, T. Sekiguchi, K. M. Itoh, D. N. Jamieson, J. C. McCallum, A. S. Dzurak, and A. Morello, Storing quantum information for 30 seconds in a nanoelectronic device, Nat. Nanotechnol. 9, 986 (2014).
- [6] J. Y. Huang, R. Y. Su, W. H. Lim, M. Feng, B. van Straaten, B. Severin, W. Gilbert, N. Dumoulin Stuyck, T. Tanttu, S. Serrano, J. D. Cifuentes, I. Hansen, A. E. Seedhouse, E. Vahapoglu, R. C. C. Leon, N. V. Abrosimov, H.-J. Pohl, M. L. W. Thewalt, F. E. Hudson, C. C. Escott, N. Ares, S. D. Bartlett, A. Morello, A. Saraiva, A. Laucht, A. S. Dzurak, and C. H. Yang, High-fidelity spin qubit operation and algorithmic initialization above 1 K, Nature 627, 772 (2024).
- [7] P. Steinacker, N. Dumoulin Stuyck, W. H. Lim, T. Tanttu, M. Feng, S. Serrano, A. Nickl, M. Candido, J. D. Cifuentes, E. Vahapoglu, S. K. Bartee, F. E. Hudson, K. W. Chan, S. Kubicek, J. Jussot, Y. Canvel, S. Beyne, Y. Shimura, R. Loo, C. Godfrin, B. Raes, S. Baudot, D. Wan, A. Laucht, C. H. Yang, A. Saraiva, C. C. Escott, K. De Greve, and A. S. Dzurak, Industrycompatible silicon spin-qubit unit cells exceeding 99% fidelity, Nature (2025).
- [8] C. H. Yang, K. W. Chan, R. Harper, W. Huang, T. Evans, J. C. C. Hwang, B. Hensen, A. Laucht, T. Tanttu, F. E. Hudson, S. T. Flammia, K. M. Itoh, A. Morello, S. D. Bartlett, and A. S. Dzurak, Silicon qubit fidelities approaching incoherent noise limits via pulse engineering, Nat. Electron. 2, 151 (2019).
- [9] K. Takeda, A. Noiri, T. Nakajima, J. Yoneda, T. Kobayashi, and S. Tarucha, Quantum tomography of an entangled three-qubit state in silicon, Nat. Nanotechnol. 16, 965 (2021).
- [10] A. Ruffino, T.-Y. Yang, J. Michniewicz, Y. Peng, E. Charbon, and M. F. Gonzalez-Zalba, A cryo-CMOS chip that integrates silicon quantum dots and multiplexed dispersive readout electronics, Nat. Electron. 5, 53 (2022).
- [11] S. G. J. Philips, M. T. Madzik, S. V. Amitonov, S. L. de Snoo, M. Russ, N. Kalhor, C. Volk, W. I. L. Lawrie, D. Brousse, L. Tryputen, B. P. Wuetz, A. Sammak, M. Veldhorst, G. Scappucci, and L. M. K. Vandersypen, Universal control of a six-qubit quantum processor in silicon, Nature 609, 919 (2022).
- [12] C.-A. Wang, V. John, H. Tidjani, C. X. Yu, A. S. Ivlev, C. Déprez, F. van Riggelen-Doelman, B. D. Woods, N. W. Hendrickx, W. I. L. Lawrie, L. E. A. Stehouwer, S. D. Oosterhout, A. Sammak, M. Friesen, G. Scappucci, S. L. de Snoo, M. Rimbach-Russ, F. Borsoi, and M. Veldhorst, Operating semiconductor quantum processors with hopping spins, Science 385, 447 (2024).
- [13] M. T. Madzik, S. Asaad, A. Youssry, B. Joecker, K. M. Rudinger, E. Nielsen, K. C. Young, T. J. Proctor, A. D.

- Baczewski, A. Laucht, V. Schmitt, F. E. Hudson, K. M. Itoh, A. M. Jakob, B. C. Johnson, D. N. Jamieson, A. S. Dzurak, C. Ferrie, R. Blume-Kohout, and A. Morello, Precision tomography of a three-qubit donor quantum processor in silicon, Nature 601, 348 (2022).
- [14] I. Thorvaldson, D. Poulos, C. M. Moehle, S. H. Misha, H. Edlbauer, J. Reiner, H. Geng, B. Voisin, M. T. Jones, M. B. Donnelly, L. F. Peña, C. D. Hill, C. R. Myers, J. G. Keizer, Y. Chung, S. K. Gorman, L. Kranz, and M. Y. Simmons, Grover's algorithm in a four-qubit silicon processor above the fault-tolerant threshold, Nat. Nanotechnol. 20, 472 (2025).
- [15] H. Edlbauer, J. Wang, A. M. S.-E. Huq, I. Thorvald-son, M. T. Jones, S. H. Misha, W. J. Pappas, C. M. Moehle, Y.-L. Hsueh, H. Bornemann, S. K. Gorman, Y. Chung, J. G. Keizer, L. Kranz, and M. Y. Simmons, An 11-qubit atom processor in silicon., Preprint at https://arxiv.org/abs/2506.03567 (2025).
- [16] H. G. Stemp, S. Asaad, M. R. v. Blankenstein, A. Vaartjes, M. A. I. Johnson, M. T. Mądzik, A. J. A. Heskes, H. R. Firgau, R. Y. Su, C. H. Yang, A. Laucht, C. I. Ostrove, K. M. Rudinger, K. Young, R. Blume-Kohout, F. E. Hudson, A. S. Dzurak, K. M. Itoh, A. M. Jakob, B. C. Johnson, D. N. Jamieson, and A. Morello, Tomography of entangling two-qubit logic operations in exchange-coupled donor electron spin qubits, Nat. Commun. 15, 8415 (2024).
- [17] C. D. Hill, E. Peretz, S. J. Hile, M. G. House, M. Fuechsle, S. Rogge, M. Y. Simmons, and L. C. L. Hollenberg, A surface code quantum computer in silicon, Sci. Adv. 1, e1500707 (2015).
- [18] G. Tosi, F. A. Mohiyaddin, V. Schmitt, S. Tenberg, R. Rahman, G. Klimeck, and A. Morello, Silicon quantum processor with robust long-distance qubit couplings, Nat. Commun. 8, 450 (2017).
- [19] J. Wyrick, X. Wang, P. Namboodiri, R. V. Kashid, F. Fei, J. Fox, and R. Silver, Enhanced Atomic Precision Fabrication by Adsorption of Phosphine into Engineered Dangling Bonds on H–Si Using STM and DFT, ACS Nano 16, 19114 (2022).
- [20] R. Rahman, G. P. Lansbergen, S. H. Park, J. Verduijn, G. Klimeck, S. Rogge, and L. C. L. Hollenberg, Orbital stark effect and quantum confinement transition of donors in silicon, Phys. Rev. B 80, 165314 (2009).
- [21] B. Voisin, J. Bocquel, A. Tankasala, M. Usman, J. Salfi, R. Rahman, M. Y. Simmons, L. C. L. Hollenberg, and S. Rogge, Valley interference and spin exchange at the atomic scale in silicon, Nat. Commun. 11, 6124 (2020).
- [22] S. Monir, E. N. Osika, S. K. Gorman, I. Thorvaldson, Y.-L. Hsueh, P. Macha, L. Kranz, J. Reiner, M. Y. Simmons, and R. Rahman, Impact of measurement backaction on nuclear spin qubits in silicon, Phys. Rev. B 109, 035157 (2024).
- [23] N. Yu, R. Duan, and M. Ying, Five two-qubit gates are necessary for implementing the toffoli gate, Phys. Rev. A 88, 010304 (2013).
- [24] J. J. Pla, K. Y. Tan, J. P. Dehollain, W. H. Lim, J. J. Morton, F. A. Zwanenburg, D. N. Jamieson, A. S. Dzurak, and A. Morello, High-fidelity readout and control of a nuclear spin qubit in silicon, Nature 496, 334 (2013).
- [25] J. P. Bonilla Ataides, D. K. Tuckett, S. D. Bartlett, S. T. Flammia, and B. J. Brown, The XZZX surface code, Nat. Commun. 12, 2172 (2021).
- [26] J. Roffe, L. Z. Cohen, A. O. Quintavalle, D. Chandra,

- and E. T. Campbell, Bias-tailored quantum LDPC codes, Quantum 7, 1005 (2023).
- [27] Y. Wang, A. Tankasala, L. C. L. Hollenberg, G. Klimeck, M. Y. Simmons, and R. Rahman, Highly tunable exchange in donor qubits in silicon, npj Quantum Inf. 2, 16008 (2016).
- [28] T. A. Baart, T. Fujita, C. Reichl, W. Wegscheider, and L. M. Vandersypen, Coherent spin-exchange via a quantum mediator, Nat. Nanotechnol. 12, 26 (2017).
- [29] Y. He, S. K. Gorman, D. Keith, L. Kranz, J. G. Keizer, and M. Y. Simmons, A two-qubit gate between phosphorus donor electrons in silicon, Nature 571, 371 (2019).
- [30] M. M. Munia, S. Monir, E. N. Osika, M. Y. Simmons, and R. Rahman, Superexchange coupling of donor qubits in silicon, Phys. Rev. Appl. 21, 014038 (2024).
- [31] M. R. Hogg, P. Pakkiam, S. K. Gorman, A. V. Timo-feev, Y. Chung, G. K. Gulati, M. G. House, and M. Y. Simmons, Single-shot readout of multiple donor electron spins with a gate-based sensor, PRX Quantum 4, 010319 (2023).
- [32] L. Kranz, S. Roche, S. K. Gorman, J. G. Keizer, and M. Y. Simmons, High-fidelity cnot gate for donor electron spin qubits in silicon, Phys. Rev. Appl. 19, 024068 (2023).
- [33] C. Volk, A.-M. J. Zwerver, U. Mukhopadhyay, P. T. Eendebak, C. J. van Diepen, J. P. Dehollain, T. Hensgens, T. Fujita, C. Reichl, W. Wegscheider, et al., Loading a quantum-dot based "qubyte" register, npj Quantum Information 5, 29 (2019).
- [34] A. Mills, D. Zajac, M. Gullans, F. Schupp, T. Hazard, and J. R. Petta, Shuttling a single charge across a onedimensional array of silicon quantum dots, Nature communications 10, 1063 (2019).
- [35] J. Krzywda, W. Liu, E. van Nieuwenburg, and O. Krause, Qdarts: A quantum dot array transition simulator for finding charge transitions in the presence of finite tunnel couplings, non-constant charging energies and sensor dots, SciPost Physics Codebases, 043 (2025).
- [36] M. Donnelly, J. Rowlands, L. Kranz, Y. Hsueh, Y. Chung, A. Timofeev, H. Geng, P. Singh-Gregory, S. Gorman, J. Keizer, R. Rahman, and M. Simmons, Noise correlations in an atom-based quantum dot array, Phys. Rev. Appl. 23, 064058 (2025).
- [37] Y.-H. Wu, L. C. Camenzind, P. Bütler, I. K. Jin, A. Noiri, K. Takeda, T. Nakajima, T. Kobayashi, G. Scappucci, H.-S. Goan, et al., Simultaneous highfidelity single-qubit gates in a spin qubit array, Preprint at https://arxiv.org/abs/2507.11918 (2025).
- [38] N. P. Breuckmann and J. N. Eberhardt, Quantum lowdensity parity-check codes, PRX Quantum 2, 040101 (2021).
- [39] A. O. Quintavalle, M. Vasmer, J. Roffe, and E. T. Campbell, Single-shot error correction of three-dimensional homological product codes, PRX Quantum 2, 020340 (2021).
- [40] E. Huang, A. Pesah, C. T. Chubb, M. Vasmer, and A. Dua, Tailoring three-dimensional topological codes for biased noise, PRX Quantum 4, 030338 (2023).
- [41] S. Bravyi, A. W. Cross, J. M. Gambetta, D. Maslov, P. Rall, and T. J. Yoder, High-threshold and lowoverhead fault-tolerant quantum memory, Nature 627, 778 (2024).
- [42] P. W. Shor, Scheme for reducing decoherence in quantum computer memory, Phys. Rev. A 52, R2493 (1995).

- [43] D. Gottesman, An introduction to quantum error correction and fault-tolerant quantum computation., Preprint at https://arxiv.org/abs/0904.2557 (2009).
- [44] J. Kelly, R. Barends, A. G. Fowler, A. Megrant, E. Jeffrey, T. C. White, D. Sank, J. Y. Mutus, B. Campbell, Y. Chen, Z. Chen, B. Chiaro, A. Dunsworth, I.-C. Hoi, C. Neill, P. J. J. O'Malley, C. Quintana, P. Roushan, A. Vainsencher, J. Wenner, A. N. Cleland, and J. M. Martinis, State preservation by repetitive error detection in a superconducting quantum circuit, Nature 519, 66 (2015).
- [45] S. Krinner, N. Lacroix, A. Remm, A. Di Paolo, E. Genois, C. Leroux, C. Hellings, S. Lazar, F. Swiadek, J. Herrmann, G. J. Norris, C. K. Andersen, M. Muller, A. Blais, C. Eichler, and A. Wallraff, Realizing repeated quantum error correction in a distance-three surface code, Nature 605, 669 (2022).
- [46] J. Yoneda, T. Otsuka, T. Takakura, M. Pioro-Ladrière, R. Brunner, H. Lu, T. Nakajima, T. Obata, A. Noiri, C. J. Palmstrøm, A. C. Gossard, and S. Tarucha, Robust micromagnet design for fast electrical manipulations of single spins in quantum dots, Appl. Phys. Express 8, 084401 (2015).
- [47] P. Huang and X. Hu, Spin qubit relaxation in a moving quantum dot, Phys. Rev. B 88, 075301 (2013).
- [48] T. Fujita, T. A. Baart, C. Reichl, W. Wegscheider, and L. M. K. Vandersypen, Coherent shuttle of electron-spin states, npj Quantum Inf. 3, 22 (2017).
- [49] I. Seidler, T. Struck, R. Xue, N. Focke, S. Trellenkamp, H. Bluhm, and L. R. Schreiber, Conveyor-mode singleelectron shuttling in Si/SiGe for a scalable quantum computing architecture, npj Quantum Inf. 8, 100 (2022).
- [50] V. Langrock, J. A. Krzywda, N. Focke, I. Seidler, L. R. Schreiber, and L. Cywiński, Blueprint of a scalable spin qubit shuttle device for coherent mid-range qubit transfer in disordered si/sige/sio₂, PRX Quantum 4, 020305 (2023).
- [51] R. Xue, M. Beer, I. Seidler, S. Humpohl, J.-S. Tu, S. Trellenkamp, T. Struck, H. Bluhm, and L. R. Schreiber, Si/SiGe QuBus for single electron information-processing devices with memory and micron-scale connectivity function, Nat. Commun. 15, 2296 (2024).
- [52] M. De Smet, Y. Matsumoto, A.-M. J. Zwerver, L. Tryputen, S. L. de Snoo, S. V. Amitonov, S. R. Katiraee-Far, A. Sammak, N. Samkharadze, o. Gul, R. N. M. Wasserman, E. Greplova, M. Rimbach-Russ, G. Scappucci, and L. M. K. Vandersypen, High-fidelity single-spin shuttling in silicon, Nat. Nanotechnol. 20, 866 (2025).
- [53] F. Borjans, X. G. Croot, X. Mi, M. J. Gullans, and J. R. Petta, Resonant microwave-mediated interactions between distant electron spins, Nature 577, 195 (2020).
- [54] P. Harvey-Collard, J. Dijkema, G. Zheng, A. Sammak, G. Scappucci, and L. M. K. Vandersypen, Coherent spinspin coupling mediated by virtual microwave photons, Phys. Rev. X 12, 021026 (2022).
- [55] C. X. Yu, S. Zihlmann, J. C. Abadillo-Uriel, V. P. Michal, N. Rambal, H. Niebojewski, T. Bedecarrats, M. Vinet, E. Dumur, M. Filippone, B. Bertrand, S. De Franceschi, Y.-M. Niquet, and R. Maurand, Strong coupling between a photon and a hole spin in silicon, Nat. Nanotechnol. 18, 741 (2023).
- [56] J. Dijkema, X. Xue, P. Harvey-Collard, M. Rimbach-Russ, S. L. de Snoo, G. Zheng, A. Sammak, G. Scappucci, and L. M. K. Vandersypen, Cavity-mediated iSWAP

- oscillations between distant spins, Nat. Phys. **21**, 168 (2025).
- [57] V. N. Golovach, M. Borhani, and D. Loss, Electric-dipoleinduced spin resonance in quantum dots, Phys. Rev. B 74, 165319 (2006).
- [58] Y. Tokura, W. G. van der Wiel, T. Obata, and S. Tarucha, Coherent single electron spin control in a slanting zeeman field, Phys. Rev. Lett. 96, 047202 (2006).
- [59] F. K. Unseld, B. Undseth, E. Raymenants, Y. Matsumoto, S. L. de Snoo, S. Karwal, O. Pietx-Casas, A. S. Ivlev, M. Meyer, A. Sammak, M. Veldhorst, G. Scappucci, and L. M. K. Vandersypen, Baseband control of single-electron silicon spin qubits in two dimensions, Nat. Commun. 16, 5605 (2025).
- [60] J. Salfi, J. A. Mol, D. Culcer, and S. Rogge, Charge-insensitive single-atom spin-orbit qubit in silicon, Phys. Rev. Lett. 116, 246801 (2016).
- [61] S. Zhang, Y. He, and P. Huang, Acceptor-based qubit in silicon with tunable strain, Phys. Rev. B 107, 155301 (2023).

- [62] X. Yu, B. Wilhelm, D. Holmes, A. Vaartjes, D. Schwienbacher, M. Nurizzo, A. Kringhøj, M. R. v. Blankenstein, A. M. Jakob, P. Gupta, F. E. Hudson, K. M. Itoh, R. J. Murray, R. Blume-Kohout, T. D. Ladd, N. Anand, A. S. Dzurak, B. C. Sanders, D. N. Jamieson, and A. Morello, Schrödinger cat states of a nuclear spin qudit in silicon, Nat. Phys. 21, 362 (2025).
- [63] P. Gupta, A. Vaartjes, X. Yu, A. Morello, and B. C. Sanders, Robust macroscopic schrödinger's cat on a nucleus, Phys. Rev. Res. 6, 013101 (2024).
- [64] V. Srinivasa, H. Xu, and J. M. Taylor, Tunable spin-qubit coupling mediated by a multielectron quantum dot, Phys. Rev. Lett. 114, 226803 (2015).
- [65] F. K. Malinowski, F. Martins, T. B. Smith, S. D. Bartlett, A. C. Doherty, P. D. Nissen, S. Fallahi, G. C. Gardner, M. J. Manfra, C. M. Marcus, and F. Kuemmeth, Spin of a multielectron quantum dot and its interaction with a neighboring electron, Phys. Rev. X 8, 011045 (2018).